Journal of Materials Chemistry C

ROYAL SOCIETY OF CHEMISTRY

PAPER

View Article Online
View Journal | View Issue

Cite this: J. Mater. Chem. C, 2023, 11, 14833

Thermoelectric properties of *Pnma* and *R3m* GeS and GeSe†

Min Zhang, Joseph M. Flitcroft, Sophie K. Guillemot and Jonathan M. Skelton *

Received 17th August 2023,
Accepted 9th October 2023

DOI: 10.1039/d3tc02938g

rsc.li/materials-c

With ~60% of global energy lost as heat, technologies such as thermoelectric generators (TEGs) are an important route to enhancing the efficiency of energy-intensive processes. Optimising thermoelectric (TE) materials requires balancing a set of interdependent physical properties to meet efficiency, cost and sustainability requirements, and is a complex materials-design challenge. In this study, we demonstrate a fully first-principles modelling approach to calculating the properties and thermoelectric figure of merit *ZT* and apply it to the orthorhombic and rhombohedral phases of GeS and GeSe. While p-doped *Pnma* GeS and GeSe do not match the performance of the Sn analogues, due to a smaller electrical conductivity σ and larger lattice thermal conductivity κ_{latt}, we predict a large ZT_{max} = 2.12 for n-doped *Pnma* GeSe at 900 K, which would make it a good match for p-type SnSe in a thermoelectric couple. Moreover, with n-type doping the σ is largest along the layering direction and aligns with the minimum κ_{latt}, and a much larger $ZT_{max} > 3$ could potentially be accessible with control over the growth direction. We also predict that p-doped *R3m* GeS and GeSe can achieve an industrially-viable $ZT > 1$, through a high σ counterbalanced by a large thermal conductivity, and experiments indicate this can be further improved by alloying. Our results therefore strongly motivate further study of the under-explored Ge chalcogenides as prospective TEs, with a particular focus on strategies for n-doping the *Pnma* phases.

1 Introduction

Energy underpins every aspect of modern human life. Despite substantial progress in renewable energy technologies such as wind and solar power, fossil fuels remain the leading energy resource in many countries, and demand is still increasing.[1] However, fossil fuels are a finite resource, and the CO_2 and other emissions from extracting and burning them have serious impacts on the climate and on human health.[2] To reduce our reliance on fossil fuels, it is critical both to develop a portfolio of clean energy technologies and to improve the efficiency with which we use energy.[3–7]

At present, around 60% of the energy consumed globally is wasted as heat,[8,9] which has led to substantial interest in thermoelectric generators (TEGs) to convert heat to electricity and thereby improve the efficiency of energy-intensive processes. TEGs are solid-state devices that extract electrical energy from a temperature gradient and are easily scalable to a range of applications including in the automotive, manufacturing and power-generation industries.[9] The performance of a thermoelectric material can be described by the dimensionless figure of merit *ZT*:[9]

$$ZT = \frac{S^2\sigma}{\kappa_{el} + \kappa_{latt}}T \quad (1)$$

where *S* is the Seebeck coefficient, σ is the electrical conductivity, $S^2\sigma$ is the power factor (PF), *T* is the absolute temperature, and κ_{el} and κ_{latt} are the electronic and lattice (phonon) contributions to the thermal conductivity. To first approximation, *S*, σ and κ_{el} are interrelated through the carrier concentration *n* such that the best balance of a large PF and minimal κ_{el} is typically obtained for heavily-doped semiconductors. On the other hand, κ_{latt} is largely independent of the electrical transport and must be minimised to obtain a large *ZT*.

A wide variety of inorganic materials have been explored as thermoelectric (TE) materials, including chalcogenides,[10–14] metal oxides,[15–18] clathrates,[19–22] and skutterudites.[23–26] The current

Department of Chemistry, University of Manchester, Oxford Road, Manchester M13 9PL, UK. E-mail: jonathan.skelton@manchester.ac.uk

† Electronic supplementary information (ESI) available: Impact of non-analytical corrections on the lattice thermal conductivity; comparison of electronic-structure calculations with self-consistent and non-self-consistent HSE06 and with a variety of *k*-point meshes; optimized lattice parameters and comparison to experimental measurements; phonon spectra of the three GeSe structures examined in this work; phonon spectra of *R3m* GeS obtained using different second-order supercell expansions; electronic band structure and density of states of *Pnma* and *R3m* GeS; and additional data on the electrical transport properties, lattice thermal conductivity and thermoelectric figure of merit of the four systems examined in this work, including on the anisotropy. See DOI: https://doi.org/10.1039/d3tc02938g

industry-standard TEs are Bi_2Te_3 ($ZT_{max} \approx 1$ from 359–450 K) and PbTe ($ZT_{max} = 2.2$ at 915 K).[27–29] However, Pb is toxic and Te has a low terrestrial abundance of *ca.* 1 ppb,[30] comparable to Pt, and is required for other technologies such as photovoltaics. This makes it impractical to deploy TEGs based on either material at scale.[9]

Given that chalcogenides often show the required balance of favourable electrical properties and low κ_{latt}, much research has focused on alternative compositions. The electrical properties required for a high-performance TE are similar to those needed for many other optoelectronic applications, and the Sn and Ge monochalcogenides SnS/SnSe and GeS/GeSe have both been widely explored as absorber materials for thin-film solar cells.[31–36] SnSe has been identified as an extremely promising TE material with an ultra-high bulk $ZT_{max} \approx 2.6$ at 923 K,[37] a good ZT over a wide temperature range of 300–773 K,[38] and an even higher polycrystalline $ZT_{max} \approx 3.1$ at 773 K.[39] SnS shows very similar structural chemistry to SnSe, and is advantageous due to the higher abundance and lower toxicity of S, but has yet to demonstrate comparable TE performance.[40–42]

The Ge chalcogenides exhibit similar structures and optoelectronic properties to the Sn analogues, but their TE performance is less well characterised. However, Ge is 1000× more abundant than Te and less toxic than Pb,[43] making GeS and GeSe attractive as prospective TEs. A small number of computational studies have predicted the orthorhombic *Pnma* phase of GeSe to have a large $ZT_{max} = 2.5$ at 800 K, competitive with SnSe, and *Pnma* GeS to attain $ZT_{max} = 0.73$ at 700 K, close to the industry-standard $ZT = 1$.[44,45] More recently, the *R*3*m* phase of GeSe was also reported to show a $ZT > 1$.[46]

In our previous work on the tin chalcogenides we developed a workflow for calculating the four parameters in the ZT equation (eqn (1)) from first principles, which was found to give accurate predictions for the well-characterised *Pnma* SnS and SnSe.[11] In this work, we apply a similar approach to predict the electrical and thermal transport properties of the *Pnma* and *R*3*m* phases of GeS and GeSe, with good agreement to available experimental data.[47–50] By considering both p- and n-type doping, we predict that n-type *Pnma* GeSe has the highest potential ZT_{max} of 2.12 at 900 K, at a realistic doping level of 6×10^{19} cm^{-3}, which would make it a good partner for p-type SnSe in a thermoelectric couple. Moreover, the n-doped material is predicted to show the largest σ and lowest κ_{latt} along the layered *b* direction, potentially yielding a much larger $ZT > 3$ if the growth direction can be controlled. We also predict that the *R*3*m* phases can potentially attain $ZT > 1$ at mid-to-high temperature, which experiments suggest can be improved by suppressing the κ_{latt} through alloying.

2 Computational methods

Pseudopotential plane-wave density–functional theory (DFT) calculations were performed using the Vienna *ab initio* Simulation Package (VASP) code.[51]

Initial crystal structures of *Pnma* GeS and GeSe were taken from ref. 52, and the *R*3*m* structures of the two chalcogenides were derived from the GeTe structure reported in ref. 53 by replacing the chalcogen atom. The rocksalt structure of GeSe was taken from ref. 54, and rocksalt GeS was prepared from this by substituting Se with S.

All six structures were fully optimized using a plane-wave cutoff of 550 eV and tight tolerances of 10^{-8} eV and 10^{-2} eV Å^{-1} on the electronic total energy and forces, respectively. The dispersion-corrected PBEsol+D3 method[55,56] was chosen to model the electron exchange and correlation based on our previous work.[57,58] Projector-augmented wave (PAW) pseudopotentials[59,60] were used to model the ion cores with the following valence configurations: Ge $3d^{10}4s^24p^2$; S $3s^23p^4$; and Se $4s^24p^4$. Γ-centred Monkhort-Pack ***k***-point meshes with $7 \times 3 \times 9$, $7 \times 7 \times 7$ ($7 \times 7 \times 2$) and $10 \times 10 \times 10$ ($6 \times 6 \times 6$) subdivisions were used to sample the Brillouin zones of the *Pnma* and primitive (conventional) *R*3*m* and rocksalt unit cells, respectively.

Supercell finite-displacement phonon calculations were performed using the Phonopy package,[61] and the lattice thermal conductivities were computed using the Phono3py code.[62] The second-order (harmonic) force constants were obtained using a displacement step of 10^{-2} Å with $4 \times 2 \times 4$, $4 \times 4 \times 2$ and $3 \times 3 \times 3$ supercell expansions of the *Pnma*, *R*3*m* and rocksalt conventional cells, respectively, containing 256, 192 and 216 atoms. The third-order (anharmonic) force constants for the *Pnma* and *R*3*m* structures were obtained using a displacement step of 3×10^{-2} Å with $2 \times 1 \times 2$ and $3 \times 3 \times 1$ supercells containing 32 and 54 atoms. (As explained below, we did not attempt thermal-conductivity or electronic-structure calculations on the rocksalt structures due to the presence of imaginary modes in the phonon spectra.) During post-processing, transformation matrices were applied to the *R*3*m* and rocksalt structures to transform to the primitive cells.

To evaluate the atom-projected phonon density of states (PDoS) curves, the phonon frequencies were interpolated onto uniform Γ-centered ***q***-point meshes with $28 \times 13 \times 36$, $28 \times 28 \times 28$, and $40 \times 40 \times 40$ subdivisions for the *Pnma*, *R*3*m*, and rocksalt phases, respectively. The phonon dispersion curves were evaluated by interpolating the frequencies onto strings of ***q***-points passing through the high-symmetry points in the respective Brillouin zones. Non-analytical corrections at $\boldsymbol{q} \rightarrow \Gamma$ were included to model the splitting between the longitudinal and transverse optic modes (*i.e.*, LO/TO splitting) using the approach in ref. 63. The required Born effective charges $\boldsymbol{Z}^{\star}$ and high-frequency dielectric constants $\boldsymbol{\varepsilon}_{\infty}$ were computed using PBEsol+D3 and density–functional perturbation theory (DFPT).[64] The κ_{latt} was calculated within the single-mode relaxation-time approximation (SM-RTA) based on modal properties calculated on Γ-centered ***q***-point meshes with $16 \times 8 \times 16$ and $24 \times 24 \times 24$ subdivisions for the *Pnma* and *R*3*m* phases, respectively. We found that LO/TO splitting has a negligible impact on the κ_{latt} of the four systems (Fig. S1, ESI†).

Electronic-structure calculations were performed using the HSE06 hybrid functional[65] to obtain accurate electronic bandgaps E_g and were used as the basis to model the electronic transport properties with the AMSET code.[66]

Uniform band structures were calculated using PBEsol+D3 and ***k***-point meshes with two times the number of subdivisions

along each reciprocal lattice vector as the meshes used for the geometry optimisations (2.5× for *R*3*m* GeS), and a scissors operator applied to increase the E_g to the HSE06 values. Four scattering mechanisms were considered to determine the electronic relaxation times, *viz.* acoustic deformation potential (ADP), piezoelectric (PIE), polar optical phonon (POP), and ionized impurity (IMP) scattering. The high-frequency dielectric constants $\boldsymbol{\varepsilon}_\infty$ were obtained as the real part of the energy-dependent dielectric function $\boldsymbol{\varepsilon}(E) = \boldsymbol{\varepsilon}_{re}(E) + i\boldsymbol{\varepsilon}_{im}(E)$ at $E = 0$. The $\boldsymbol{\varepsilon}(E)$ were calculated using HSE06 within the independent-particle approximation, from a sum over transitions between occupied and virtual electronic states,[64] and with the number of bands in the calculations increased to 2× and 3× the defaults for the *Pnma* and *R*3*m* phases, respectively, to ensure convergence. The static dielectric constants, elastic constants and piezoelectric moduli were obtained using the finite-difference routines in VASP with PBEsol+D3. The POP frequency was obtained from the Γ-point phonon frequencies and the $\boldsymbol{Z}^*$ determined using PBEsol+D3 and DFPT.[64] We note that PIE scattering is only relevant for the *R*3*m* systems, since the *Pnma* structure is centrosymmetric and the piezoelectric moduli vanish by symmetry.

For the HSE06 calculations, the semi-core Ge 3d electrons were subsumed into the pseudopotential cores, which we found had very little impact on the electronic-structure calculations but significantly reduced the computational cost of the hybrid calculations. Whereas the $\boldsymbol{k}$-point meshes used for the geometry optimisations were sufficient to converge the E_g and $\boldsymbol{\varepsilon}_\infty$ of the *Pnma* phases, explicit testing indicated that denser sampling was required in calculations on the *R*3*m* phases. For these systems, we therefore employed the non-self-consistent approach documented in previous work,[67] after verifying that the E_g and $\boldsymbol{\varepsilon}_\infty$ obtained using both methods and the "base" $\boldsymbol{k}$-point meshes gave quantitatively similar results. Convergence tests and a comparison of the self-consistent and non-self-consistent HSE06 calculations can be found in Section 1 of the ESI.†

3 Results and discussion

3.1 Structures and lattice dynamics

A feature of the group IV–VI chalcogenides is the rich structural chemistry related to the stereochemical activity of the tetrel lone pairs.[57,58,68] Under ambient conditions, GeS and GeSe both adopt the "pseudo 2D" layered Herzenbergite structure formed by SnS and SnSe with the orthorhombic *Pnma* space-group (Fig. 1(a)). *Pnma* GeSe is also known to transform to the rhombohedral phase (space group *R*3*m*; Fig. 1(b)) adopted by GeTe under low hydrostatic pressure.[69] GeSe has also been proposed to form the cubic rocksalt structure (space group $Fm\bar{3}m$; Fig. 1(c)) adopted by the Pb chalcogenides at elevated temperature and under pressure.[69,70] A variety of other monochalcogenide phases are also reported,[71,72] but we focus here on the *Pnma*, *R*3*m* and rocksalt phases.

In the high-symmetry cubic $Fm\bar{3}m$ structure both the tetrel and chalcogen atoms occupy six-fold coordinated octahedral sites.

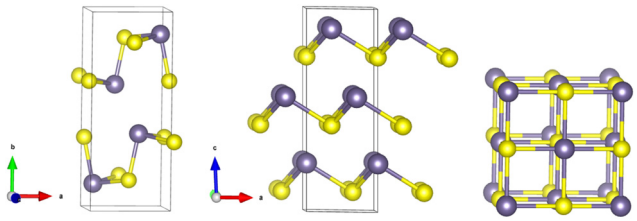

Fig. 1 Structures of the *Pnma* (a), *R*3*m* (b), and rocksalt ($Fm\bar{3}m$) (c) phases of GeS and GeSe. Purple and yellow spheres denote the Ge and chalcogen atoms, respectively. The *R*3*m* and $Fm\bar{3}m$ structures are shown in the conventional cells. These figures were generated using VESTA.[74]

The rhombohedral *R*3*m* structure is derived from the rocksalt structure by a small displacement of the cations from their ideal positions, which results in both atoms forming three short and three long bonds. The *Pnma* phase can be considered a further distortion to the rocksalt structure in which every other unit cell along the *b* axis is offset, resulting in a pseudo 2D layered structure in which the Ge and S atoms each form two short and one long bond. This structure enables the Ge^{2+} cations to have an active $4s^2$ lone pair, which projects into the interlayer space and supports a van der Waals interaction between adjacent layers.[73]

The optimized lattice constants are compared to previous reports in Table S3 in the ESI.† The lattice parameters for the *Pnma* phases are in good agreement with previous measurements.[54,75] The lattice parameters for rocksalt and *R*3*m* GeSe are underestimated by 3.5% and 2.5% compared to experiments, which we attribute to the measurements in ref. 54 and 50 being carried out at finite temperature and therefore including an appreciable amount of thermal expansion compared to our "athermal" DFT optimisations.[58] There are some discrepancies between our calculations on the *R*3*m* and rocksalt phases and other theoretical work,[76,77] which we attribute primarily to the tendency of the PBE functional employed in these studies to overestimate lattice constants and cell volumes compared to PBEsol+D3.

The phonon dispersion and density of states (DoS) curves of the *Pnma*, *R*3*m* and rocksalt phases of GeS are shown in Fig. 2. The unit cell of *Pnma* phase contains $n_a = 8$ atoms, and the primitive cells of the *R*3*m* and rocksalt phases contain $n_a = 2$ atoms, resulting in $3n_a = 24$ and $3n_a = 6$ branches at each wavevector $\boldsymbol{q}$ in the respective phonon dispersions. The phonon dispersion of *Pnma* GeS, with the most phonon bands, is notably more complex than those of the *R*3*m* and rocksalt phases. The lower symmetry of the *R*3*m* phase and consequent lower band degeneracy also results in a more complex phonon spectrum than for the rocksalt structure. The atom-projected DoS (PDoS) curves for *Pnma* and *R*3*m* GeS show that the lower- and higher-frequency modes are dominated by motions of heavier Ge and lighter S, respectively. *Pnma* GeS also shows a clear separation between the 12 lower- and higher-frequency modes and a prominent "phonon bandgap". In contrast, while the PDoS of rocksalt GeS also shows a low-frequency feature dominated by Ge motion, there is considerable overlap between Ge and S at higher frequencies.

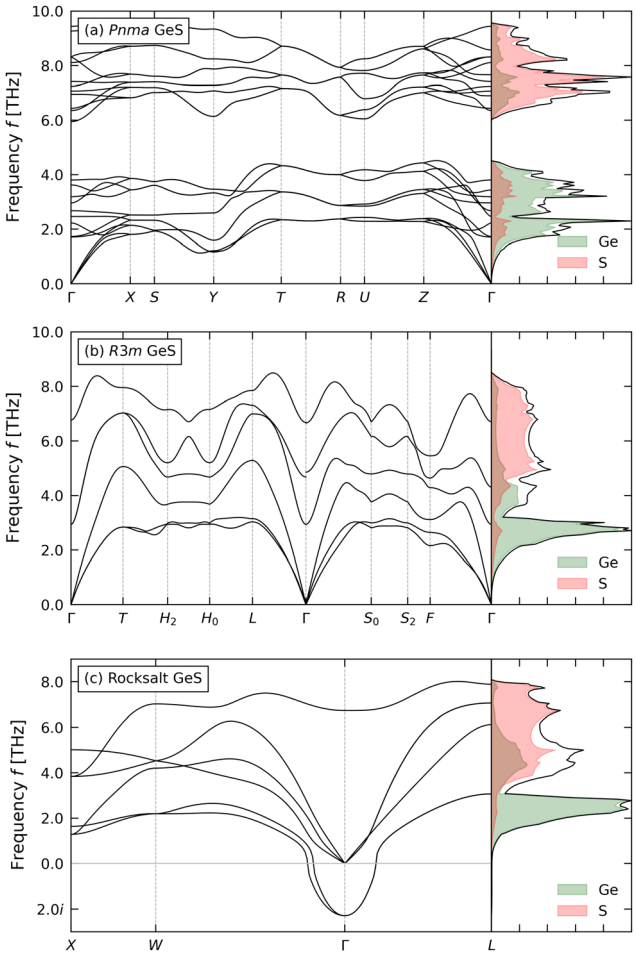

Fig. 2 Phonon dispersion and density of states (DoS) curves of (a) *Pnma*, (b) *R3m*, and (c) rocksalt GeS. In each DoS plot, the total DoS is shown by a black line and the atom-projected DoS (PDoS) of the Ge and S atoms is shown by green and red shaded curves.

The calculated phonon spectra of the three GeSe phases (Fig. S4, ESI†) show similar features, with the notable exception that the PDoS of *Pnma* and *R3m* GeSe shows contributions from both atoms across the full range of phonon frequencies. Similarly, while there is some "splitting" in the PDoS of rocksalt GeSe, it is less prominent than in GeS. The extent of the splitting can be attributed to both the mass differences between Ge and S/Se, and to the nature of the bonding in the different structure types. Comparison of the spectra of GeS and GeSe also shows that the latter span a narrower range of frequencies, which is primarily due to the inverse relationship between frequency and atomic mass.

Whereas the phonon dispersion curves of both pairs of *Pnma* and *R3m* structures show real frequencies across the Brillouin zone, the two rocksalt structures show prominent imaginary modes at the $\boldsymbol{q}$ = Γ wavevector, indicating that the high-symmetry cubic phase is dynamically unstable. The position of the imaginary modes further indicates that the energy-lowering distortion can be represented in the primitive cell, and therefore likely corresponds to a cation off-centering to the *R3m* structure. This in turn suggests that the high-temperature rocksalt structure observed in experiments may be a crystallographic average over locally-distorted *R3m* domains. The predicted dynamical stability of *Pnma* GeS/GeSe and *R3m* GeSe is consistent with previous studies,[76–78] as is the instability of rocksalt GeSe.[79]

There is, however, an interesting contrast with the analagous rocksalt SnS and SnSe. Rocksalt SnS is dynamically unstable under ambient conditions, but the imaginary mode lies at $\boldsymbol{q}$ = *X* rather than $\boldsymbol{q}$ = Γ, indicating a different type of energy-lowering distortion.[57,58] In contrast to both SnS and GeSe, rocksalt SnSe is dynamically stable.[58]

The calculations in ref. 76 predicted *R3m* GeS to be dynamically unstable with a small imaginary mode along the Γ → *X* and Γ → *L* directions in the phonon dispersion. We attribute this discrepancy to an overestimation of the unit-cell volume with PBE, which has been shown in some cases to introduce unphysical imaginary modes into phonon spectra.[80] Nevertheless, to rule out possible technical issues, we tested a series of second-order supercell expansions containing 300–648 atoms, but did not observe imaginary modes in any of these calculations (Fig. S5, ESI†).

Given the dynamical instability of the rocksalt structures, we focus on the *Pnma* and *R3m* phases in the remainder of this study.

3.2 Electronic transport properties

The calculated electronic band structures and density of states (DoS) curves of *Pnma* and *R3m* GeSe are presented in Fig. 3, and those of GeS are presented in Fig. S6 (ESI†). For both *Pnma* phases the conduction band minima (CBM) and valence band maxima (VBM) lie at different points along the Γ → *X* direction, resulting in indirect bandgaps of E_g = 1.32 and 1.17 eV for GeS and GeSe, respectively. The CBM and VBM of the two *R3m* phases are both located at the $\boldsymbol{k}$ = *L* wavevector, as in the rocksalt Pb and Sn chalcogenides,[11,81] resulting in a direct gap of E_g = 0.3 eV for both systems. These predictions are generally in very good agreement with experimental measurements and previous calculations.[49,82–85] We note, however, that previous computational studies on *R3m* GeS and GeSe predicted much larger E_g,[77,86] which we attribute to insufficiently dense $\boldsymbol{k}$-point meshes (*cf.* Table S2 and Fig. S2/S3, ESI†). The calculated bandgaps of *Pnma* GeS and GeSe are larger than the 0.93 and 0.82 eV predicted for *Pnma* SnS and SnSe in our previous work.[11] On the other hand, the E_g of the *R3m* phases are considerably smaller than the 0.6 eV we predicted for rocksalt SnS and SnSe,[11] which suggests the rhombohedral distortion in GeS and GeSe may lead to a significant narrowing of the gap.

Having verified our calculated bandgaps, the electronic-structure calculations were used as the basis for electronic-transport calculations using semi-classical Boltzmann transport theory and an approximate model of the electron relaxation times.[66,87]

The transport properties are determined from the spectral conductivity $\boldsymbol{\Sigma}$ and the *n*th-order moments of the generalised transport coefficients $\mathscr{L}^n$ given by:[66,88]

$$\boldsymbol{\Sigma}(\varepsilon, T) = \sum_j \int \frac{1}{8\pi^3} \boldsymbol{\nu}_{\boldsymbol{k}j} \otimes \boldsymbol{\nu}_{\boldsymbol{k}j} \tau_{\boldsymbol{k}j}(T) \delta[\varepsilon - \varepsilon_{\boldsymbol{k}j}] \mathrm{d}\boldsymbol{k} \qquad (2)$$

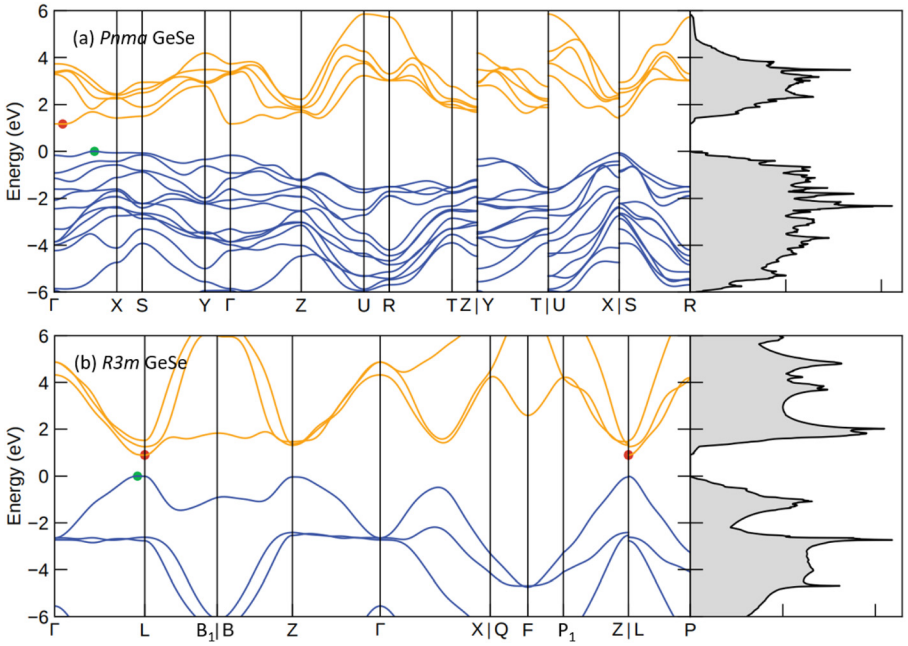

Fig. 3 Electronic band structures and density of states (DoS) of (a) *Pnma* and (b) *R3m* GeSe obtained using the HSE06 hybrid functional. On each band structure, the valence and conduction bands are shown in blue and orange, respectively, the valence-band maximum and conduction-band minimum (VBM/CBM) are marked by green and red circles, and the VBM is set to 0 eV.

$$\mathscr{L}^n(T) = e^2 \int \boldsymbol{\Sigma}(\varepsilon, T)(\varepsilon - \varepsilon_F)^n \left[-\frac{\partial f^0(\varepsilon, T)}{\partial \varepsilon} \right] \mathrm{d}\varepsilon \qquad (3)$$

The $\varepsilon_{\boldsymbol{k}j}$, $\boldsymbol{\nu}_{\boldsymbol{k}j}$ and $\tau_{\boldsymbol{k}j}$ are the energies, group velocities and relaxation times, respectively, of electrons with wavevector $\boldsymbol{k}$ and band index j. e is the elementary charge. $f^0(\varepsilon,T)$ is the Fermi–Dirac distribution given by:

$$f^0(\varepsilon, T) = \frac{1}{\exp[(\varepsilon - \varepsilon_F)/k_B T] + 1} \qquad (4)$$

where ε_F is the Fermi energy and k_B is the Boltzmann constant.

The $\varepsilon_{\boldsymbol{k}j}$ and $\boldsymbol{\nu}_{\boldsymbol{k}j}$ are obtained from a high-quality electronic-structure calculation. The electron relaxation times $\tau_{\boldsymbol{k}j}$ in eqn (2) are computed from four scattering processes, *viz.* acoustic deformation potential (ADP), piezoelectric (PIE), polar optical phonon (POP) and ionised impurity (IMP) scattering, according to Matthiessen's Rule:

$$\frac{1}{\tau_{\boldsymbol{k}j}(T)} = \frac{1}{\tau^{\mathrm{ADP}}_{\boldsymbol{k}j}(T)} + \frac{1}{\tau^{\mathrm{PIE}}_{\boldsymbol{k}j}(T)} + \frac{1}{\tau^{\mathrm{POP}}_{\boldsymbol{k}j}(T)} + \frac{1}{\tau^{\mathrm{IMP}}_{\boldsymbol{k}j}(T)} \qquad (5)$$

where we note that the inverse lifetimes are the scattering rates. The four rates are estimated from a number of material properties, and full details are given in ref. 66.

With the $\boldsymbol{\Sigma}$ and $\mathscr{L}^n$ defined, the three electrical properties in eqn (1) can be calculated according to:

$$\boldsymbol{\sigma} = \mathscr{L}^0 \qquad (6)$$

$$\boldsymbol{S} = \frac{1}{eT} \frac{\mathscr{L}^1}{\mathscr{L}^0} \qquad (7)$$

$$\boldsymbol{\kappa}_{\mathrm{el}} = \frac{1}{e^2 T} \left[\frac{(\mathscr{L}^1)^2}{\mathscr{L}^0} - \mathscr{L}^2 \right] \qquad (8)$$

where we have omitted the explicit temperature dependence of the transport properties and the $\mathscr{L}^n$ for brevity.

The electrical properties are calculated for a set of specified temperatures and extrinsic carrier concentrations n ("doping levels"), which together determine the Fermi energy ε_F in eqn (3) and (4). We selected a temperature range of 300–900 K, with room temperature being the practical lower limit for most thermoelectric applications and 900 K close to the highest of the reported phase-transition temperatures of *Pnma* GeS and GeSe (863 and 907 K, respectively).[44,70] A range of doping levels between $n = 10^{16}$–10^{20} cm^{-3} was chosen to bracket the intrinsic carrier concentration of 10^{16} cm^{-3} reported for GeSe[89] and the $n \approx 5 \times 10^{19}$ cm^{-3} reported in experiments on doped SnSe.[38,39,90,91] Experiments on the Ge and Se chalcogenides typically target p-type (hole) doping, which is readily achieved in SnSe *e.g.* by substituting Sn with Ag or Na,[38,39] or by promoting Sn vacancies.[90,91] However, n-type (electron) doping has also been reported for both SnS and SnSe,[92,93] and has been predicted to lead to favourable properties in *Pnma* GeS.[45] We therefore considered both types of doping. We note that the n is set by adjusting the position of the Fermi energy E_F in the electronic-structure calculations, and the calculations therefore do not consider the practicality or potential effect of incorporating the defects or dopants at the concentration required to achieve a target doping level.

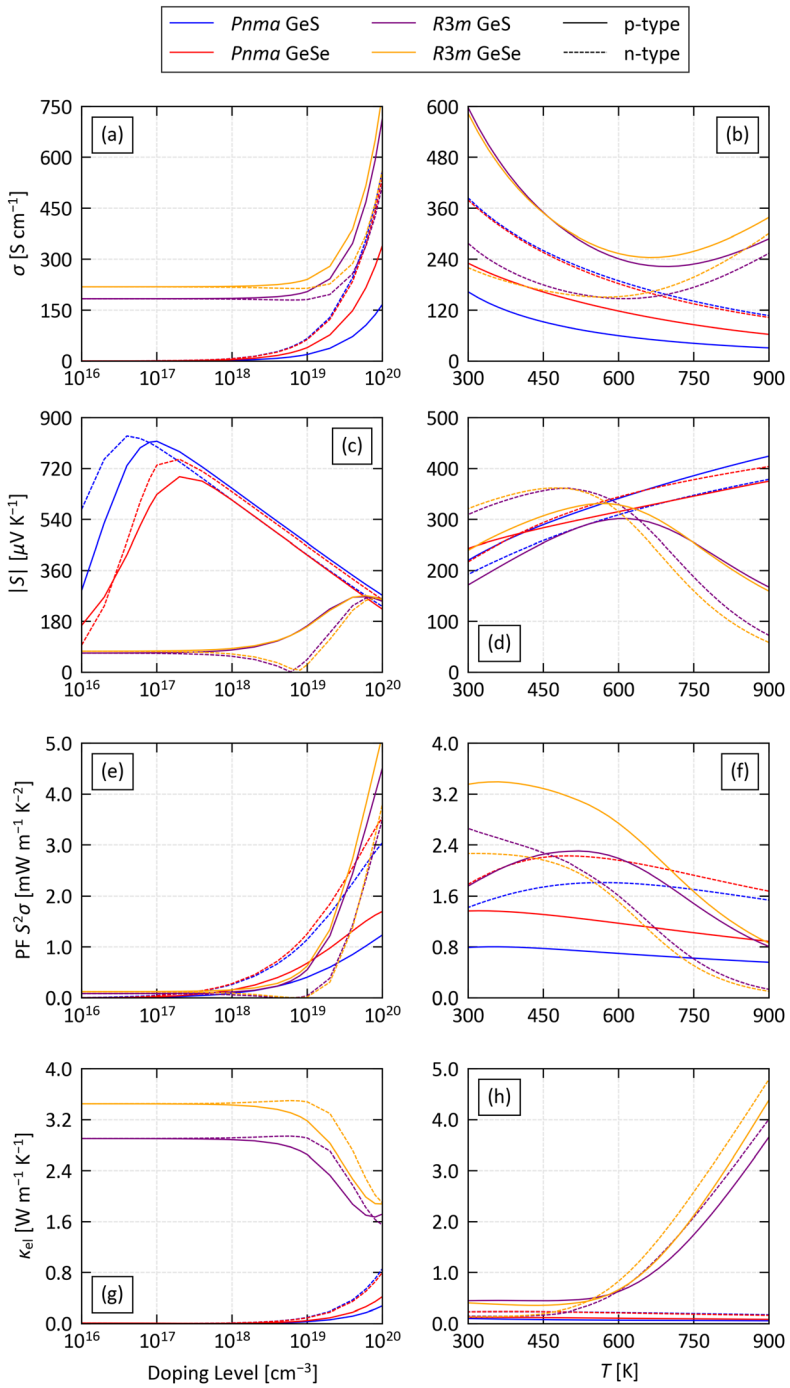

Fig. 4 (a)/(b) Averaged electrical conductivity σ, (c)/(d) averaged absolute Seebeck coefficient $|S|$, (e)/(f) averaged power factor $S^2\sigma$ and (g)/(h) averaged electronic thermal conductivity κ_{el} of the four structures examined in this work. Each property is obtained with p-type (solid lines) and n-type doping (dashed lines), both (a)/(c)/(e)/(g) as a function of carrier concentration n at a fixed T = 800 K and (b)/(d)/(f)/(h) as a function of temperature at a fixed $n = 2 \times 10^{19}$ cm^{-3}.

The $\boldsymbol{\sigma}$, $\boldsymbol{S}$, and $\boldsymbol{\kappa}_{el}$ are 3 × 3 tensors in which the diagonal components correspond to transport along the principal x, y and z directions. TEGs are typically based on thin films or pressed/sintered pellets composed of randomly-oriented crystal grains, and we therefore focus mainly on the scalar averages of the diagonal elements, which we denote S, σ and κ_{el} to distinguish them from the tensor quantities.

Fig. 4 compares the averaged electrical conductivity σ, absolute Seebeck coefficient $|S|$, thermoelectric power factor $S^2\sigma$ (PF) and electronic thermal conductivity κ_{el} of the four systems, for both p- and n-type doping. We first performed an analysis of the transport properties as a function of doping level at a fixed T = 800 K, chosen to be slightly below the reported phase-transition temperatures of *Pnma* GeS and GeSe.[44,70] At this temperature, the PFs

of *Pnma* GeS and GeSe are negligible up to $n \approx 10^{18}$ cm^{-3} and then increase rapidly with the doping level (Fig. 4(e)). Comparison with the Seebeck coefficient and conductivity shows that this is due to an exponential-like increase in σ at large n, which compensates a monotonic fall in the S from the peak values around $n = 10^{17}$ cm^{-3} (Fig. 4(a) and (c)). Interestingly, the calculations predict that n-type doping leads to comparable or larger S and 2–3× larger σ than p-type doping, resulting in a much larger PF.

The narrow bandgap of the *R*3*m* phases results in large intrinsic p-type conductivity that dominates the electrical properties up to $n \approx 10^{17}$ cm^{-3}. Above this, both the σ and S increase with larger doping levels, and the increase in the electrical conductivity results in a steep rise in the PF above $n \approx 10^{19}$ cm^{-3}. Similar behaviour was also predicted for rocksalt SnS and SnSe in our previous work.[11] The S of the *R*3*m* phases is smaller than the *Pnma* phases at low n but comparable at large n. The σ obtained with p-type doping is larger than in the p-doped *Pnma* phases over the range of n tested, resulting in a 3–4× larger PF at $n = 10^{20}$ cm^{-3}. n-type doping produces a smaller σ, comparable to the n-doped *Pnma* systems, and the balance of the smaller S and steeper dependence of the σ on n results in lower PFs than predicted for the n-doped *Pnma* systems at most doping levels.

The *Pnma* phases are predicted to have comparable and low κ_{el}, increasing with the conductivity to maximum values of ~0.4 and 0.8 W m^{-1} K^{-1} for GeS and GeSe, respectively, at the largest $n = 10^{20}$ cm^{-3} we tested (Fig. 4(g)). On the other hand, the intrinsic p-type conductivity of the *R*3*m* systems results in a much larger κ_{el}, of around 3 and 3.5 W m^{-1} K^{-1} for *R*3*m* GeS and GeSe, respectively, which reduces to 1.6–2 W m^{-1} K^{-1} at large n. This indicates a somewhat complex relationship between the carrier concentration, σ and κ_{el} in the *R*3*m* systems, but is again similar to our previous calculations on rocksalt SnS and SnSe.[11]

At a fixed $n = 2 \times 10^{19}$ cm^{-3}, which is a conservative estimate of the achievable p-type doping levels in SnSe,[38,39,90,91] the PFs of p-doped *Pnma* GeS and GeSe show a slow decrease, while the $S^2\sigma$ of the n-doped phases peak at intermediate temperature and fall at higher T (Fig. 4(f)). In both cases, this is a product of a reduction in the σ with temperature and a rise in the S (Fig. 4(b) and (d)). On the other hand, at this n the S of the two *R*3*m* phases are predicted to fall with temperature, leading to a significant drop in the PFs at higher T.

The reduction in σ with temperature predicted for the *Pnma* phases is typical of a degenerate semiconductor, *i.e.* a heavily-doped semiconductor that exhibits metallic-like behaviour, and so one might expect the electrical thermal conductivity to follow the Wiedemann–Franz law:

$$\kappa_{el} = L\sigma T \quad (9)$$

where L is the Lorentz number. In these systems, the decrease in σ counteracts the increase in T to produce a relatively flat temperature dependence of the κ_{el} (Fig. 4(h)). On the other hand, the κ_{el} of the *R*3*m* phases are predicted to rise sharply above around 500–600 K, from <1 W m^{-1} K^{-1} to ~3.5–4.5 W m^{-1} K^{-1} at $T = 900$ K. The σ of the *R*3*m* phases is predicted to fall at low temperature, reach a minimum at intermediate T, and rise at higher T, and the latter would combine with the T term in eqn (9) to produce this behaviour.

We also investigated the anisoptropy in the electronic transport of the four systems (Fig. S7–S14, ESI†). The Seebeck coefficients of the *Pnma* phases are predicted to be relatively isotropic for $n > 5 \times 10^{17}$ cm^{-3}. On the other hand, the calculations predict strong anisotropy in the σ. In the p-doped systems, the in-plane conductivity along the a and c directions is up to 2–3× higher than along the layered b direction, while, conversely, in the n-doped systems the interlayer conductivity along the b direction is more than 5× higher than along the in-plane directions. This anisotropy is reflected in the power factors, and is largely preserved across the 300–900 K temperature range with a fixed $n = 2 \times 10^{19}$ cm^{-3}. In contrast to the *Pnma* phases, the transport in the *R*3*m* phases is relatively isotropic. The largest discrepancies are that the Seebeck coefficients of the p- and n-doped systems are smaller and larger along the c direction, respectively, but the relatively small absolute values of the S mean the anisotropy in the PFs is minimal.

Finally, we also examined the electron scattering rates for both p- and n-type doping at $n = 2 \times 10^{19}$ cm^{-3} and $T = 800$ K (Fig. 5 and Fig. S15–S18, ESI†). POP scattering generally dominates close to the Fermi energy, with additional contributions from PIE scattering in the *R*3*m* phases. ADP scattering becomes dominant at energies above the conduction-band minimum in the n-doped *Pnma* phases, and also at energies below and above the VBM/CBM in the p- and n-doped *R*3*m* phases, respectively, while for the p-doped *Pnma* phases IMP scattering is predicted to be significant at energies below the VBM.

The modelling approach employed here previously yielded accurate predictions for SnS and SnSe.[11] While the Ge chalcogenides are not as well characterised, the present calculations appear to show similarly good agreement with available experimental measurements. The measurements on *Pnma* $Ge_{0.79}Ag_{0.01}Sn_{0.2}Se$ in ref. 47 obtained $S \approx 300$ μV K^{-1} at 300 K with $n \approx 5 \times 10^{18}$ cm^{-3}, and we predict the same 300 K Seebeck coefficient with a 2× larger $n = 10^{19}$ cm^{-3}. The measurements on *R*3*m* $(GeSe)_{0.9}(AgBiTe_2)_{0.1}$ in ref. 49 reported $S \approx 151$ and

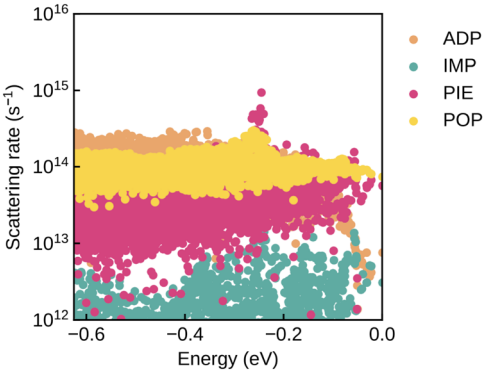

Fig. 5 Calculated scattering rates as a function of energy for p-doped *R*3*m* GeSe at a doping level of $n = 2 \times 10^{19}$ cm^{-3} and temperature $T = 800$ K.

250 μV K^{-1} at room temperature and 723 K, and a PF of 1.28 mW m^{-1} K^{-2} at 627 K, all with a carrier concentration of 1.1 × 10^{19} cm^{-3}. With a comparable n = 10^{19} cm^{-3} we predict a power factor of 1.47 mW m^{-1} K^{-2} at 620 K and a S = 287 and 218 μV K^{-1} at 300 and 720 K, which we again consider to be reasonable agreement given that the experimental sample is an alloy. (We note that our calculations predict a very similar S = 156 and 251 μV K^{-1} at the two temperatures with increased carrier concentrations of 8 × 10^{19} cm^{-3} and 10^{20} cm^{-3}, respectively).

3.3 Lattice thermal conductivity

Within the single-mode relaxation-time approximation (SM-RTA), the macroscopic lattice thermal conductivity $\boldsymbol{\kappa}_{\text{latt}}$ is calculated as a sum of contributions from microscopic phonon modes $\lambda = \boldsymbol{q}j$ according to:[62]

$$\boldsymbol{\kappa}_{\text{latt}} = \frac{1}{N}\sum_{\lambda}\boldsymbol{\kappa}_{\lambda}(T) = \frac{1}{NV}\sum_{\lambda}C_{\lambda}(T)\boldsymbol{\nu}_{\lambda}\otimes\boldsymbol{\nu}_{\lambda}\tau_{\lambda}(T) \qquad (10)$$

$\boldsymbol{q}$ and j are the phonon wavevector and band index respectively. V is the unit-cell volume and N is the number of $\boldsymbol{q}$ included in the summation, which is equivalent to the number of unit cells in the crystal. The C_{λ} and $\boldsymbol{\nu}_{\lambda}$ are the modal heat capacities and group velocities, respectively, and are calculated within the harmonic approximation. The τ_{λ} are the phonon lifetimes, calculated as the inverse of the phonon linewidths Γ_{λ}:

$$\tau_{\boldsymbol{q}j}(T) = \frac{1}{\Gamma_{\boldsymbol{q}j}(T)} \qquad (11)$$

The Γ_{λ} are themselves calculated from the harmonic phonon frequencies and displacement vectors (eigenvectors) and the third-order force constants. Full details of this method can be found in ref. 62.

The calculated scalar-averaged κ_{latt} of the four Ge chalcogenides is shown in Fig. 6(a). Given that the ultra-low lattice thermal conductivity of SnSe is a key contributor to its high thermoelectric performance,[37,94–96] we also compare our predictions to similar calculations on SnS and SnSe.[97] The κ_{latt} span a range of 0.82–1.71 W m^{-1} K^{-1} at 800 K (Table 1) and fall in the order of *R3m* GeSe > *Pnma* GeS ≈ *R3m* GeS > *Pnma* GeSe ≈ *Pnma* SnS > *Pnma* SnSe. The orthorhombic Ge chalcogenides therefore have larger κ_{latt} than the Sn analogues, but *Pnma* GeSe has a κ_{latt} comparable to SnS.

As for the electrical properties, the averaged κ_{latt} is likely to be of most relevance to thermoelectric devices. However, *Pnma* SnS and SnSe both show strongly-anisotropic thermal transport,[97] which is an important contributor to the "headline" *ZT* in single-crystal SnSe,[37] so we also examined the anisotropy in the $\boldsymbol{\kappa}_{\text{latt}}$ of the four systems (Table 1 and Fig. S19–S22, ESI†). The symmetry of the *R3m* structure is such that $\kappa_{xx} = \kappa_{yy} \neq \kappa_{zz}$, and the independent κ_{xx} and κ_{zz} are similar and close to the average. For the *Pnma* structures, on the other hand, we predict strong anisotropy such that the lowest κ_{latt} is obtained along the layered b axes (κ_{yy}) and the highest along the strongly-bonded c axes (κ_{zz}). Indeed, the anisotropy is so large that while *Pnma* and *R3m* GeS are predicted to have similar averaged κ_{latt} of 1.23 and 1.11 W m^{-1} K^{-1}, respectively, at 800 K, the κ_{latt} of the *Pnma* phase is an average over three values that range from 0.50 W m^{-1} K^{-1} along the b direction to 2.35 W m^{-1} K^{-1} along the c axis.

Again as for the electrical properties, our predictions of the lattice thermal conductivity are generally in good agreement with experimental measurements and other calculations. Our predicted 300 K κ_{latt} = 2.18 W m^{-1} K^{-1} for *Pnma* GeSe compares favourably to the measured values of 1.8–2.9 W m^{-1} K^{-1}.[47,49,50] The axial components are also similar to reported values of 2.3, 0.64–1.11 and 4.8 W m^{-1} K^{-1} along the a, b and c directions.[44,50,98,99] At a higher T = 700 K, our predicted average value of 0.92 W m^{-1} K^{-1} is also comparable to the 0.85 W m^{-1} K^{-1} reported in ref. 50. We note that our calculated κ_{latt} of *Pnma* GeS and GeSe are substantially larger than the minimum values of 0.52 and 0.39 W m^{-1} K^{-1} predicted by the approximate model in ref. 100, but the poor agreement with previous experimental and theoretical studies on GeSe suggest this model does not make realistic predictions. On the other hand, the predicted κ_{latt} = 0.98 W m^{-1} K^{-1} along the b direction of *Pnma* GeS at T = 700 K predicted in ref. 45 is much larger than our predicted 0.56 W m^{-1} K^{-1}, which we attribute to the use of PBE and a smaller 64-atom supercell to compute the force constants.

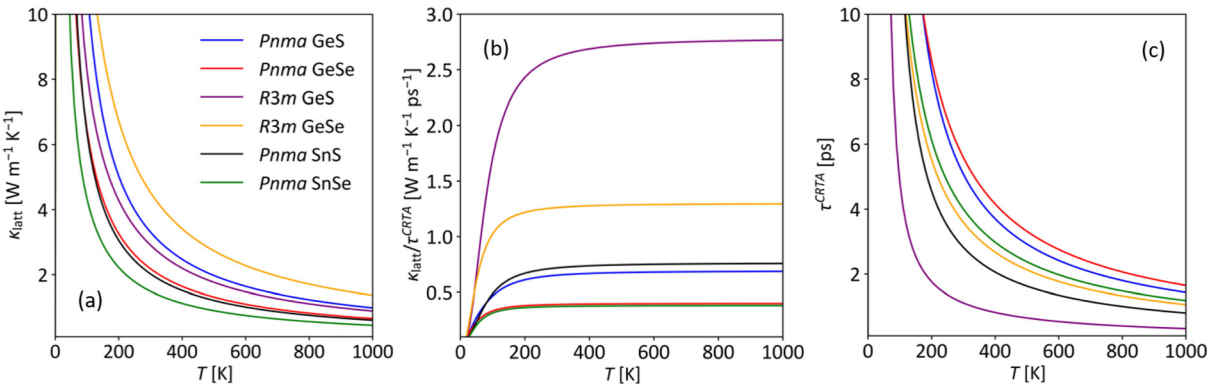

Fig. 6 Lattice thermal conductivity of *Pnma* and *R3m* GeS/GeSe and *Pnma* SnS/SnSe: averaged lattice thermal conductivity κ_{latt} (a) and constant relaxation-time approximation (CRTA) decomposition into an averaged harmonic component $\kappa_{\text{latt}}/\tau^{\text{CRTA}}$ (b) and averaged lifetime τ^{CRTA} (c) as defined in eqn (12). The data on SnS and SnSe was taken from our previous work.[97]

Table 1 Calculated lattice thermal conductivity $\boldsymbol{\kappa}_{\text{latt}}$ of the *Pnma* and *R3m* phases of GeS and GeSe at T = 800 K. The three diagonal components κ_{xx}, κ_{yy} and κ_{zz}, corresponding to transport along the x, y, and z directions, respectively, are shown together with the average κ_{ave}. We also show the averaged harmonic and lifetime components $\kappa/\tau^{\text{CRTA}}$ and τ^{CRTA} calculated according to eqn (12) and the average phonon–phonon interaction strength $\tilde{P}_\lambda$ for each model. Data for *Pnma* SnS and SnSe from the similar calculations in ref. 97 are also given for comparison

	$\boldsymbol{\kappa}_{\text{latt}}$ [W m^{-1} K^{-1}]						
	κ_{xx}	κ_{yy}	κ_{zz}	κ_{ave}	$\kappa/\tau^{\text{CRTA}}$ [W m^{-1} K^{-1} ps^{-1}]	τ^{CRTA} [ps]	$\tilde{P}_\lambda$ [10^{-8} eV^2]
GeS (*Pnma*)	0.85	0.50	2.35	1.23	0.68	1.80	3.06
GeSe (*Pnma*)	0.72	0.30	1.45	0.82	0.40	2.06	1.43
GeS (*R3m*)	1.15	1.15	1.03	1.11	2.76	0.40	7.37
GeSe (*R3m*)	1.83	1.83	1.47	1.71	1.29	1.32	1.87
SnS (*Pnma*)[97]	0.71	0.51	1.20	0.80	0.75	1.07	2.62
SnSe (*Pnma*)[97]	0.61	0.35	0.81	0.59	0.38	1.56	1.10

Our predicted 300 K κ_{latt} = 4.53 W m^{-1} K^{-1} for *R3m* GeSe is similar to the 4.88 W m^{-1} K^{-1} obtained in previous calculations,[101] whereas we attribute the lower values obtained from the calculations in ref. 77 to an overestimation of the lattice constants with PBE. We were only able to find experimental measurements on polycrystalline *R3m* $(GeSe)_{0.9}(AgBiSe_2)_{0.1}$,[46,49] which report lattice thermal conductivities of 0.74, 0.38 and 0.47 W m^{-1} K^{-1} at 300, 578 and 723 K, respectively. While these are much lower than our predicted 4.53, 2.36 and 1.95 W m^{-1} K^{-1}, this can be attributed at least partially to the established impact of alloying on the κ_{latt}.[97,102–105]

Having shown that our predicted $\boldsymbol{\kappa}_{\text{latt}}$ are in good agreement with comparable measurements, we used the analysis techniques developed in our previous work[19,23,97] to investigate the origin of the differences between the systems.

We first rewrite the $\boldsymbol{\kappa}_{\text{latt}}$ as the product of a harmonic term and a weighted-average phonon lifetime τ^{CRTA} according to:

$$\begin{aligned}\boldsymbol{\kappa}_{\text{latt}}(T) &\approx \tau^{\text{CRTA}}(T) \times \frac{1}{NV}\sum_{\lambda}\frac{\boldsymbol{\kappa}_\lambda(T)}{\tau_\lambda(T)} \\ &= \tau^{\text{CRTA}}(T) \times \frac{1}{NV}\sum_{\lambda} C_\lambda(T)\boldsymbol{\nu}_\lambda \otimes \boldsymbol{\nu}_\lambda\end{aligned} \tag{12}$$

Fig. 6(b) and (c) compare the harmonic components and averaged lifetimes of the four Ge chalcogenides to SnS and SnSe. The $\kappa/\tau^{\text{CRTA}}$ rapidly approaches a constant value as the C_λ saturate to the Dulong-Petit limit, such that above ~400 K this function is indicative of differences in the group velocities $\boldsymbol{\nu}_\lambda$. Comparison of the $\kappa/\tau^{\text{CRTA}}$ reveal three trends, *viz.* that the $\boldsymbol{\nu}_\lambda$ are smaller in the *Pnma* phases than in the *R3m* phases, are around 50% smaller for the selenides than the sulphides, and are similar for GeS/SnS and GeSe/SnSe. The latter implies that the tetrel atom has little impact on the group velocities.

In contrast, the τ^{CRTA} are strongly temperature dependent, and the sharp reduction in the phonon lifetimes with temperature, due to larger phonon occupation numbers and stronger scattering, dominates the behaviour of the κ_{latt} once the $\kappa/\tau^{\text{CRTA}}$ reach the limiting values. *Pnma* GeS and GeSe have similar averaged lifetimes, so differences in the κ_{latt} are due to the group velocities. *R3m* GeS and GeSe both have shorter τ^{CRTA} than the corresponding *Pnma* phases. The averaged lifetimes of GeS are shorter than those of GeSe, which compensates for the higher $\boldsymbol{\nu}_\lambda$, and, somewhat counter-intuitively, results in a smaller overall predicted κ_{latt} for the sulphide than the selenide. The two Sn chalcogenides both have shorter averaged lifetimes than the equivalent Ge phases, resulting in smaller $\boldsymbol{\kappa}_{\text{latt}}$ despite the similar $\kappa/\tau^{\text{CRTA}}$. This indicates that, while the tetrel atoms have a minimal effect on the group velocities, they do have an impact on the $\boldsymbol{\kappa}_{\text{latt}}$ through the phonon lifetimes.

The τ^{CRTA} can be further written as the product of a set of averaged modal (anharmonic) three-phonon interaction strengths, P_λ, and a counting function $N_2(\boldsymbol{q},\omega)$ that captures the number of allowed energy- and (crystal) momentum-conserving scattering pathways (termed the "scattering phase space").[19] A comparison between systems can be made by calculating a weighted-average interaction strength, $\tilde{P}$, and a function $\bar{N}_2$ that shows the size of the scattering phase space (average number of scattering pathways) as a function of phonon frequency only. Full details can be found in our previous work.[19,23,97] The $\tilde{P}$ were determined at 800 K as described in our previous work[23,97] (Fig. S23–S26, ESI†). Scaled $\tilde{P}$ and $\bar{N}_2$ that can be compared between systems are provided in Table 1 and Fig. 7 respectively. (Unscaled $\bar{N}_2$ for the four systems examined in this work, showing separate contributions from collision and decay pathways, are shown in Fig. S27–S30 in the ESI†).

The calculated $\tilde{P}$ of the *Pnma* Ge and Sn chalcogenides range from 1.10–3.06 × 10^{-8} eV^2. The averaged interaction strengths are slightly higher in the Ge chalcogenides, and around 2× larger in the sulphides than the selenides. The calculated $\tilde{P}$ of *R3m* GeSe is ~30% larger than that of *Pnma* GeSe, but the averaged interaction strength in rhombohedral GeS is a much larger 2× that of *Pnma* GeS. Taking the $\tilde{P}$ as a measure of the intrinsic phonon anharmonicity, this analysis shows that the sulphides are more anharmonic than the selenides, the Ge chalcogenides are more anharmonic than the Sn analogues, and the *R3m* phases are more anharmonic than the *Pnma* structures.

The trends in anharmonicity are balanced by the $\bar{N}_2$, which show that the scattering phase spaces are larger for the Sn chalcogenides than the Ge analogues, larger for the selenides than the sulphides, and larger for the *Pnma* phases than the *R3m* phases, at least at low frequencies where modes typically contribute most to the κ_{latt}. The longer averaged lifetimes of *Pnma* GeSe and SnSe compared to the respective sulphides indicate that the larger $\bar{N}_2$ do not fully compensate for the smaller $\tilde{P}$. On the other hand, the smaller $\tilde{P}$ of *Pnma* SnS and SnSe is more than compensated by the larger $\bar{N}_2$ and results in

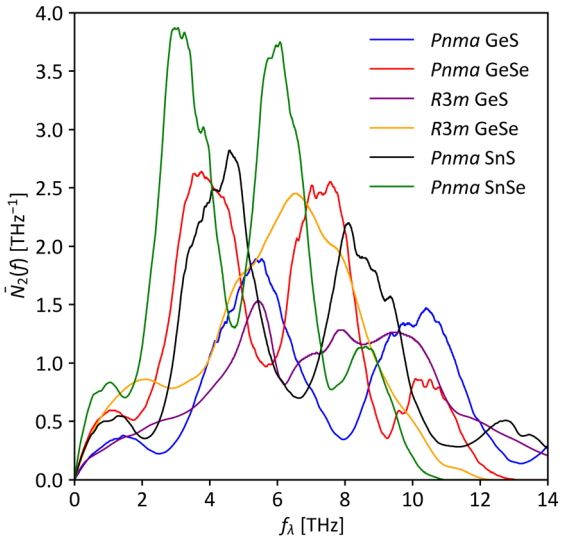

Fig. 7 Calculated averaged weighted joint density of states (w-JDoS) functions $\bar{N}_2$ at 800 K for the four Ge chalcogenides examined in this work compared to data on orthorhombic SnS and SnSe from ref. 97.

both Sn chalcogenides having shorter lifetimes than the Ge analogues. For the *R*3*m* phases, while GeSe has a larger $\bar{N}_2$ than GeS this does not compensate for the much larger $\tilde{P}$ in the sulphide, resulting in the selenide having a $\sim$3.2$\times$ longer τ^{CRTA}.

3.4 Thermoelectric figure of merit

We now combine our calculated electrical properties $\boldsymbol{S}$, $\boldsymbol{\sigma}$ and $\boldsymbol{\kappa}_{el}$ with the calculated $\boldsymbol{\kappa}_{latt}$ to obtain the figure of merit $\boldsymbol{ZT}$ as a function of doping level and temperature using eqn (1) (Fig. 8 and Fig. S31–S34, ESI†).

As in previous sections we mainly focus on the averaged *ZT*. The ZT_{max} for the four p- and n-doped Ge chalcogenides and *Pnma* SnS/SnSe,[11,97] at temperatures below the reported phase transition temperatures (GeS: 863 K, GeSe: 907 K, SnS: 878 K, SnSe: 750 K[37,44,70,106–108]), are summarised in Table 2 and S4 (ESI†).

The ZT_{max} of the *Pnma* phases are all achieved at higher doping levels and temperatures. Higher *n* maximise the electrical conductivity, which dominates the power factor $S^2\sigma$, while the shallow temperature dependence of the power factor $S^2\sigma$ and electronic thermal conductivity κ_{el} mean that the reduction in κ_{latt} favours higher *T* (*cf.* Fig. 4 and 6(a)). In contrast, the ZT_{max} of the *R*3*m* phases occur at the largest $n = 10^{20}$ cm^{-3} we tested but at lower *T*. In these systems, larger n maximises the *S*, σ and PF and reduces the κ_{el}, whereas the mid-temperature

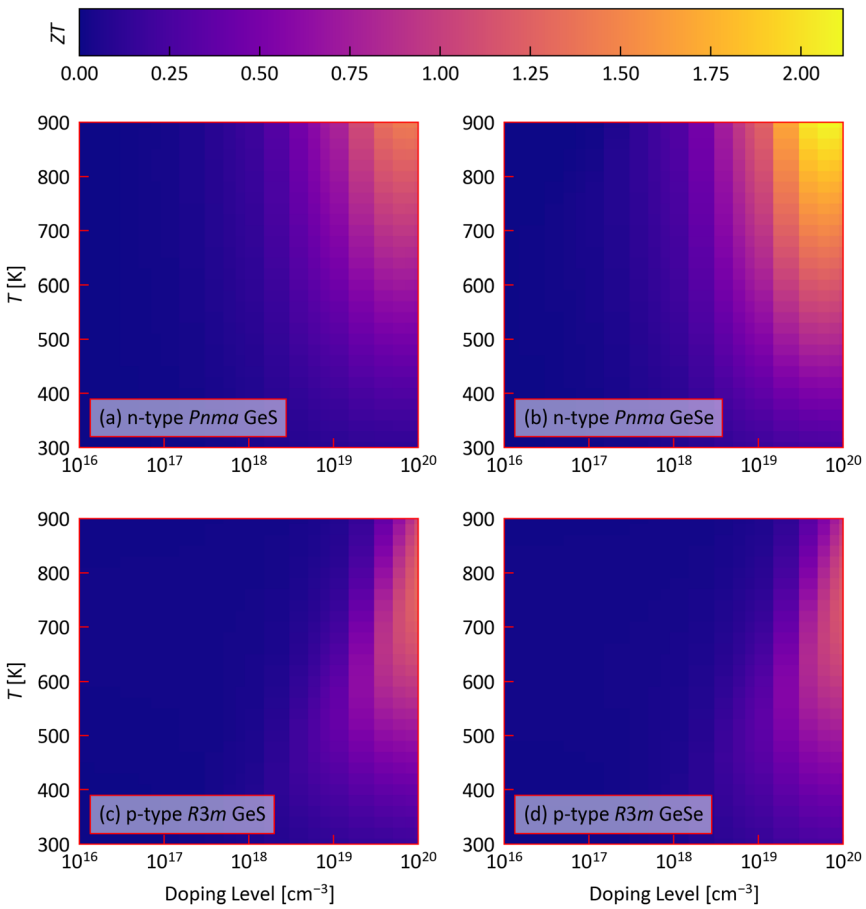

Fig. 8 Calculated scalar-averaged figure of merit *ZT* of (a) n-type *Pnma* GeS, (b) n-type *Pnma* GeSe, (c) p-type *R*3*m* GeS, and (d) p-type *R*3*m* GeSe as a function of doping level n and temperature *T*.

Table 2 Predicted maximum thermoelectric figure of merit, ZT_{max}, of the *R3m* and *Pnma* phases of GeS and GeSe for temperatures up to the reported phase transitions in the orthorhombic phases. Separate values are provided for both p- and n-type doping together with the corresponding temperature, carrier concentration n and properties in eqn (1), *viz.* the electrical conductivity σ, Seebeck coefficient S, power factor (PF) $S^2\sigma$, electronic and lattice contributions to the thermal conductivity $\kappa_{el}/\kappa_{latt}$, and total thermal conductivity κ_{tot}. We also show data for *Pnma* SnS and SnSe from our previous study for comparison[11,97]

		n [cm^{-3}]	T [K]	ZT	σ [S cm^{-1}]	S [μV K^{-1}]	PF $S^2\sigma$ [mW m^{-1} K^{-2}]	κ [W m^{-1} K^{-1}]		
								κ_{el}	κ_{latt}	κ_{tot}
GeS (*Pnma*)	p-type	10^{20}	860	0.75	150	286	1.23	0.27	1.14	1.41
	n-type	8×10^{19}	860	1.33	415	−260	2.81	0.67	1.14	1.81
GeSe (*Pnma*)	p-type	8×10^{19}	900	1.33	229	260	1.55	0.32	0.73	1.05
	n-type	6×10^{19}	900	2.12	287	−313	2.81	0.46	0.73	1.19
GeS (*R3m*)	p-type	10^{20}	760	1.29	759	247	4.65	1.57	1.16	2.73
	n-type	10^{20}	660	1.22	605	−261	4.11	0.88	1.34	2.22
GeSe (*R3m*)	p-type	10^{20}	740	1.20	858	253	5.49	1.55	1.85	3.40
	n-type	10^{20}	700	0.96	612	−265	4.31	1.20	1.95	3.15
SnS (*Pnma*)[11,97]	p-type	3.16×10^{19}	860	1.39	226	279	1.76	0.34	0.75	1.09
	n-type	4×10^{19}	860	1.78	400	−259	2.68	0.55	0.75	1.30
SnSe (*Pnma*)[11,97]	p-type	3.16×10^{19}	740	2.07	399	272	2.96	0.42	0.64	1.06
	n-type	2×10^{19}	740	2.39	450	−289	3.75	0.52	0.64	1.16

maximum in the PF and the opposing increase and decrease in the κ_{el} and κ_{latt}, respectively, at higher temperatures produce a ZT_{max} between 650–750 K.

We predict all four n-doped *Pnma* phases, *i.e.* GeS/GeSe as well as SnS/SnSe, to show larger ZT_{max} than can be obtained with p-type doping. This is due to the anisotropy in the transport properties. With p-type doping, the σ and PFs are largest along the *a* and *c* directions but the ZT is limited by the larger κ_{latt} along these directions. With n-type doping, the most facile electrical transport is along the layered *b* direction and is therefore "aligned" with the minimum in the κ_{latt}. This results in a large ZT_{max} along the *b* direction and a larger averaged ZT than obtained with p-type doping. We discuss the anisotropy in the figure of merit of the *Pnma* phases below.

For *Pnma* SnS and SnSe, we predict n-type doping to lead to 28% and 15% larger ZT_{max} than p-type doping, whereas the ZT_{max} of *Pnma* GeS and GeSe are predicted to be 77% and 59% larger with n-type doping. *Pnma* GeSe and SnSe are predicted to have superior TE performance to the corresponding sulfides with 77% and 49% larger ZT_{max} with p-type doping and 59% and 34% larger ZT_{max} with n-type doping. This is due to a combination of a generally larger σ and comparable or larger S, leading to comparable or larger PFs, and lower total thermal conductivity.

On the other hand, p-doped *R3m* GeS and GeSe are predicted to show larger ZT_{max} than with n-type doping. *R3m* GeS is predicted to have an 8% higher ZT_{max} than *R3m* GeSe due to the larger predicted κ_{latt} of the selenide outweighing the larger PF.

The predicted n required to obtain the ZT_{max} of SnS and SnSe are comparable to the carrier concentrations achieved in experiments,[38,39,90,91] and these studies suggest the larger n required to optimise the ZT of the p-type Ge chalcogenides may also be achievable. Studies on n-doped SnS for PV applications have demonstrated $n \approx 10^{18}$ in halogen-doped single crystals and $n \approx 5 \times 10^{18}$ cm^{-3} in $Sn_{1-x}Pb_xS$ thin films,[92] while the recent study in ref. 93 achieved $n \approx 10^{19}$ cm^{-3} in $Sn_{0.95}Se$ with 1% $HfCl_4$. We therefore tentatively suggest that the lower n required to achieve the predicted ZT_{max} in the n-doped chalcogenides may be achievable with further optimisation.

Of all the system considered, *Pnma* SnSe has the highest predicted average ZT_{max} of 2.07 and 2.39 with p- and n-type doping, respectively, while n-type GeSe is predicted to attain a ZT_{max} of 2.12 comparable to p-type SnSe. This would potentially make n-type GeSe a good match for p-type SnSe in a thermoelectric couple. Although the ZT_{max} of the two *R3m* phases are not competitive with the *Pnma* systems, they are predicted to attain an industrially-viable mid-to-high temperature $ZT > 1$, which may make them useful for some applications. It is also worth noting that the highly-anisotropic electrical and thermal transport in the *Pnma* phases means a larger ZT_{max} could be obtained if the growth direction could be controlled. For p-doped GeS, the largest ZT = 1.18 is along the layered *b* direction, where the κ_{latt} is minimised, whereas in p-doped GeSe the largest ZT = 1.68 is obtained along the *a* direction, which balances a smaller κ_{latt} with more favourable electrical properties. For n-type doping, the largest PF and smallest σ are both obtained along the layered *b* direction, producing large ZT of 1.85 and 3.03.

Interestingly, the synergy between the electrical and thermal transport with n-type doping is also predicted for the *Pnma* Sn chalcogenides (Table S4, ESI†). We predict ZT_{max} of 2.91 and 4.32 for SnS and SnSe, respectively, along the layered b axes, which are 60% and 80% larger than the averaged values of 1.78 and 2.39. (This may be compared with the p-type ZT_{max} of 1.56 and 2.29 along the *c* directions, which are both ∼10% larger than the average values of 1.39 and 2.07.) Given that successful n-type doping of both SnS and SnSe has been demonstrated, and at comparable n to what we predict is needed,[93] this is also a potentially significant finding.

We briefly discuss a key approximation made in these calculations. The electrical-transport properties are calculated under the assumption that doping does not significantly change the host electronic band structure, termed the ''rigid-band approximation'' (RBA). While the RBA is to some extent a practical necessity, calculations on hole-doped PbTe found that the lowering of the band degeneracy with explicit doping led to a reduction in the calculated S on the order of 5–10%.[109] Given the lower symmetry and band degeneracy of the *Pnma* and *R*3*m* phases, we might expect a smaller effect in the systems examined in the present study. We also note that the methodology we use for the electrical-transport calculations has been explicitly tested against heavily-doped systems and found to give good results.[66] A further consideration is the potential impact of doping on the phonon spectrum and κ_{latt}. While there has been little theoretical investigation of this, experiments on single-crystal SnS and SnSe with up to 3 at% doping, yielding hole concentrations on the order of 5×10^{19} cm^{-3}, suggest a small reduction in the κ_{latt}.[38,110] The calculations would therefore overestimate the κ_{latt}, which could partially compensate a potential overestimation of the S similar to that reported in ref. 109. Indeed, our previous work on the Sn chalcogenides, and recent work on the bismuth oxychalcogenides, suggests that the predicted ZT may benefit from a favourable cancellation of errors between the electrical and thermal transport properties.[11,111] Therefore, without explicit calculations to confirm, or otherwise, we tentatively suggest that the use of the RBA should not have too large an impact on our predicted ZT.

With this in mind, our predicted ZT for GeS and GeSe are generally a good match to previous experimental and theoretical studies.[44,47] In particular, measurements on $Ag_{0.01}Ge_{0.79}Sn_{0.2}Se$ reported a ZT of 0.2 at T = 700 K and $n \approx 10^{18}$ cm^{-3},[47] and we obtain the same figure of merit with a similar $n = 2 \times 10^{18}$ cm^{-3}. The authors also predicted a significant enhancement to ZT = 0.6 at a larger $n \approx 5 \times 10^{19}$ cm^{-3}, which is consistent with our predicted ZT = 0.87 with $n = 4 \times 10^{19}$ cm^{-3}. Previous theoretical studies have also predicted superior TE performance for n-type doping, as found in the present study.[45,99] We note, however, that our predictions show considerable quantitative differences to some previous calculations.[44,45,99,112] For example, the study on *Pnma* GeS in ref. 45 predicted a $\sim$2.5$\times$ larger κ_{latt} and 50% smaller ZT at 700 K than the present calculations, while the calculations in ref. 44 predicted a 5$\times$ larger σ, smaller κ_{el}, and 2–4$\times$ larger ZT. However, this can be put down to the considerable technical differences to the present calculations.

The comparison of our predictions for the *R*3*m* phases to experiments is rather more mixed. We predict a comparable ZT = 0.83 for GeSe at 540 K ($n = 8 \times 10^{19}$ cm^{-3}) to the ZT = 0.9 at 500 K predicted in ref. 101. On the other hand, the study in ref. 77 predicted $ZT > 2$ at 800 K and $n \approx 10^{19}$ cm^{-3}, whereas we predict $ZT < 1$ at 800 K at a larger $n = 8 \times 10^{19}$ cm^{-3} due to our higher predicted κ_{latt}. Compared to the measurements on GeSe/$AgBiSe_2$ alloys in ref. 46 and 49, our calculations predict that much larger n are required to obtain comparable ZT. This can be attributed in part to the high thermal conductivity predicted in these calculations, but we also find that we require a 4$\times$ larger n to reproduce the measured σ, which suggests the alloying may also impact the electrical properties. We note, however, that our calculations do reproduce the ZT = 0.84 at 720 K obtained for $(GeSe)_{0.85}(AgSbSe_2)_{0.15}$[48] with a reasonable $n = 4 \times 10^{19}$ cm^{-3}. We therefore suggest that further characterisation of the *R*3*m* phases, to measure the properties of the pure phases and to better understand the impact of alloying on the transport properties, is warranted.

4 Conclusions

In summary, we have used a fully first-principles modelling approach to explore the potential thermoelectric performance of the Ge chalcogenides GeS and GeSe.

Our calculations predict that *Pnma* GeS and GeSe can achieve larger ZT_{max} with n-type doping compared to the p-type doping typically targeted in experiments. The averaged ZT_{max} of 2.12 for *Pnma* GeSe is comparable to our predicted 2.07 for p-type *Pnma* SnSe and suggests n-type GeSe may make a good partner for SnSe in a thermoelectric couple. n-type doping results in the the maximum electrical conductivity and minimum κ_{latt} being aligned along the layered b direction, and we predict a much larger $ZT_{max} > 3$ for *Pnma* GeSe if the growth direction can be controlled. The same appears to be true for n-type SnSe, where the average ZT_{max} with n-doping is predicted to be 15% larger than with p-type doping and the directional ZT along the b axis is predicted to be 4.32. Our results therefore suggest that further exploration of the Ge chalcogenides, and of the possibility of n-type doping of both the Sn and Ge chalcogenides, will be a fruitful direction for future research.

The large predicted $\boldsymbol{\kappa}$ of the *R*3*m* phases means the predicted ZT_{max} are not competitive with the *Pnma* structures, but p-type doping is nonetheless predicted to achieve $ZT \approx 1$ between 650–750 K, which is promising and which may be useful for some applications. Given that experimental work on alloys suggests it may be possible to mitigate the large $\boldsymbol{\kappa}_{latt}$ and/or to enhance the electrical properties, we also suggest these materials may warrant further investigation.

Author contributions

Conceptualisation – JMS; methodology – all authors; data curation – all authors; formal analysis and investigation – all authors; writing (original draft) – MZ and JMF; writing (review and editing) – all authors; funding acquisition – JMS. All authors have read and agreed to the published version of the paper.

Conflicts of interest

There are no conflicts to declare.

Acknowledgements

We acknowledge helpful comments from Prof. Nicholas Chilton on a draft version of this manuscript. MZ is supported by a

China Scholarship Council (CSC) studentship (202006700004). JMS and JMF are supported by a UKRI Future Leaders Fellowship (MR/T043121/1), and JMS previously held a University of Manchester Presidential Fellowship. *Via* our membership of the UK's HEC Materials Chemistry Consortium, which is funded by EPSRC (EP/R029431 and EP/X035859), this work used ARCHER2 UK National Supercomputing Service (**https://www.archer2.ac.uk**). A subset of our calculations also made use of the UoM Computational Shared Facility (CSF) computing cluster, which is maintained by UoM Research IT.

References

1 N. Abas, A. Kalair and N. Khan, *Futures*, 2015, **69**, 31–49.
2 M. A. Ansari, *Renewable Sustainable Energy Rev.*, 2022, **168**, 112867.
3 W. Rahim, J. M. Skelton and D. O. Scanlon, *J. Mater. Chem. A*, 2021, **9**, 20417–20435.
4 R. Wolniak and B. Skotnicka-Zasadzień, *Energies*, 2022, **15**, 662.
5 B. Xu, J. Zhang, M. Egusquiza, D. Chen, F. Li, P. Behrens and E. Egusquiza, *Renewable Sustainable Energy Rev.*, 2021, **144**, 110880.
6 X. Xu, Q. Zhou and D. Yu, *Int. J. Hydrogen Energy*, 2022, **47**, 33677–33698.
7 R. Zailan, J. S. Lim, Z. A. Manan, S. R. W. Alwi, B. Mohammadi-ivatloo and K. Jamaluddin, *Renewable Sustainable Energy Rev.*, 2021, **148**, 111289.
8 A. Firth, B. Zhang and A. Yang, *Appl. Energy*, 2019, **235**, 1314–1334.
9 R. Freer and A. V. Powell, *J. Mater. Chem. C*, 2020, **8**, 441–463.
10 M. Rakshit, D. Jana and D. Banerjee, *J. Mater. Chem. A*, 2022, **10**, 6872–6926.
11 J. M. Flitcroft, I. Pallikara and J. M. Skelton, *Solids*, 2022, **3**, 155–176.
12 T.-R. Wei, P. Qiu, K. Zhao, X. Shi and L. Chen, *Adv. Mater.*, 2023, **35**, 2110236.
13 J. M. Skelton, *JPhys: Energy*, 2020, **2**, 025006.
14 T.-R. Wei, Y. Qin, T. Deng, Q. Song, B. Jiang, R. Liu, P. Qiu, X. Shi and L. Chen, *Sci. China: Mater.*, 2018, **62**, 8–24.
15 S. Ghosh, S. Harish, M. Ohtaki and B. B. Saha, *Mater. Today Energy*, 2020, **18**, 100492.
16 K. Brlec, K. B. Spooner, J. M. Skelton and D. O. Scanlon, *J. Mater. Chem. A*, 2022, **10**, 16813–16824.
17 Y. Feng, X. Jiang, E. Ghafari, B. Kucukgok, C. Zhang, I. Ferguson and N. Lu, *Adv. Compos. Hybrid Mater.*, 2018, **1**, 114–126.
18 S. D. Luu, T. A. Duong and T. B. Phan, *Adv. Nat. Sci.: Nanosci. Nanotechnol.*, 2019, **10**, 023001.
19 B. Wei, J. M. Flitcroft and J. M. Skelton, *Molecules*, 2022, **27**, 6431.
20 W. R. Puspita, H. Takeya, T. Mochiku, Y. Ishikawa, S. Lee, S. Torii, M. Hagihala and T. Kamiyama, 2019 2nd International Conference on Applied Engineering (ICAE), 2019, pp. 1-5.
21 H. Sato, H. Tamaki and T. Kanno, *Appl. Phys. Lett.*, 2020, **116**, 253901.
22 B. Sun, J. Zhao, Y. Li, L. Cao, Y. Yang, X. Fan, X. Liu, C. Wang, X. Huang and X. Wang, *et al.*, *J. Phys. Chem. C*, 2020, **124**, 9082–9088.
23 J. Tang and J. M. Skelton, *J. Phys.: Condens. Matter*, 2021, **33**, 164002.
24 G. Rogl, F. Garmroudi, A. Riss, X. Yan, J. Sereni, E. Bauer and P. Rogl, *Intermetallics*, 2022, **146**, 107567.
25 A. Serrano, O. Caballero-Calero, C. Granados-Miralles, G. Gorni, C. V. Manzano, M. Rull-Bravo, A. Moure, M. Martn-González and J. F. Fernández, *J. Alloys Compd.*, 2022, 167534.
26 H. Feng, Q. Deng, Y. Zhong, X. Rao, Y. Wang, J. Zhu, F. Zhang and R. Ang, *J. Mater. Sci. Technol.*, 2023, **150**, 168–174.
27 K. Biswas, J. He, I. D. Blum, C.-I. Wu, T. P. Hogan, D. N. Seidman, V. P. Dravid and M. G. Kanatzidis, *Nature*, 2012, **489**, 414–418.
28 Y.-K. Zhu, P. Wu, J. Guo, Y. Zhou, X. Chong, Z.-H. Ge and J. Feng, *Ceram. Int.*, 2020, **46**, 14994–15002.
29 H.-C. Hsieh, C.-H. Wang, W.-C. Lin, S. Chakroborty, T.-H. Lee, H.-S. Chu and A. T. Wu, *J. Alloys Compd.*, 2017, **728**, 1023–1029.
30 N. Belzile and Y.-W. Chen, *Appl. Geochem.*, 2015, **63**, 83–92.
31 Y. Mao, C. Xu, J. Yuan and H. Zhao, *J. Mater. Chem. A*, 2019, **7**, 11265–11271.
32 S.-C. Liu, Y. Yang, Z. Li, D.-J. Xue and J.-S. Hu, *Mater. Chem. Front.*, 2020, **4**, 775–787.
33 Y. Shen, Y. Zhang, J. Huo, X. Li, Z. Yan, Y. Pan, W. Sun, N. Deng and W. Kang, *J. Energy Storage*, 2023, **69**, 107958.
34 V. Krishnamurthi, H. Khan, T. Ahmed, A. Zavabeti, S. A. Tawfik, S. K. Jain, M. J. Spencer, S. Balendhran, K. B. Crozier and Z. Li, *et al.*, *Adv. Mater.*, 2020, **32**, 2004247.
35 I. Suzuki, S. Kawanishi, T. Omata and H. Yanagi, *JPhys: Energy*, 2022, **4**, 042002.
36 M. Feng, S.-C. Liu, L. Hu, J. Wu, X. Liu, D.-J. Xue, J.-S. Hu and L.-J. Wan, *J. Am. Chem. Soc.*, 2021, **143**, 9664–9671.
37 L.-D. Zhao, S.-H. Lo, Y. Zhang, H. Sun, G. Tan, C. Uher, C. Wolverton, V. P. Dravid and M. G. Kanatzidis, *Nature*, 2014, **508**, 373–377.
38 L.-D. Zhao, G. Tan, S. Hao, J. He, Y. Pei, H. Chi, H. Wang, S. Gong, H. Xu and V. P. Dravid, *et al.*, *Science*, 2016, **351**, 141–144.
39 C. Zhou, Y. K. Lee, Y. Yu, S. Byun, Z.-Z. Luo, H. Lee, B. Ge, Y.-L. Lee, X. Chen and J. Y. Lee, *et al.*, *Nat. Mater.*, 2021, **20**, 1378–1384.
40 B. Zhou, S. Li, W. Li, J. Li, X. Zhang, S. Lin, Z. Chen and Y. Pei, *ACS Appl. Mater. Interfaces*, 2017, **9**, 34033–34041.
41 B. Cai, L.-D. Zhao and J.-F. Li, *et al.*, *J. Materiomics*, 2020, **6**, 77–85.
42 Y. Liu, P. D. McNaughter, F. Azough, X. Liu, J. M. Skelton, A. V. Kretinin, D. J. Lewis and R. Freer, *ACS Appl. Energy Mater.*, 2023, **6**, 4462–4474.
43 J. Burton, F. Culkin and J. Riley, *Geochim. Cosmochim. Acta*, 1959, **16**, 151–180.

44 S. Hao, F. Shi, V. P. Dravid, M. G. Kanatzidis and C. Wolverton, *Chem. Mater.*, 2016, **28**, 3218–3226.
45 M. Rakshit, S. Nath, S. Chowdhury, R. Mondal, D. Banerjee and D. Jana, *Phys. Scr.*, 2022, **97**, 125804.
46 D. Sarkar, T. Ghosh, S. Roychowdhury, R. Arora, S. Sajan, G. Sheet, U. V. Waghmare and K. Biswas, *J. Am. Chem. Soc.*, 2020, **142**, 12237–12244.
47 X. Zhang, J. Shen, S. Lin, J. Li, Z. Chen, W. Li and Y. Pei, *J. Materiomics*, 2016, **2**, 331–337.
48 Y. Yu, C. Zhou, T. Ghosh, C.-F. Schön, Y. Zhou, S. Wahl, M. Raghuwanshi, P. Kerres, C. Bellin and A. Shukla, *et al.*, *Adv. Mater.*, 2023, 2300893.
49 D. Sarkar, S. Roychowdhury, R. Arora, T. Ghosh, A. Vasdev, B. Joseph, G. Sheet, U. V. Waghmare and K. Biswas, *Angew. Chem., Int. Ed.*, 2021, **60**, 10350–10358.
50 Z. Huang, S. A. Miller, B. Ge, M. Yan, S. Anand, T. Wu, P. Nan, Y. Zhu, W. Zhuang and G. J. Snyder, *et al.*, *Angew. Chem., Int. Ed.*, 2017, **56**, 14113–14118.
51 G. Kresse and J. Hafner, *Phys. Rev. B: Condens. Matter Mater. Phys.*, 1993, **47**, 558.
52 H. Wiedemeier, H. Georg and G. von Schnering, *Z. Kristallogr. - Cryst. Mater.*, 1978, **148**, 295–304.
53 P. Bauer Pereira, I. Sergueev, S. Gorsse, J. Dadda, E. Müller and R. P. Hermann, *Phys. Status Solidi B*, 2013, **250**, 1300–1307.
54 H. Wiedemeier and P. Siemers, *Zeitschrift für Anorganische und Allgemeine Chemie*, 1975, **411**, 90–96.
55 J. P. Perdew, A. Ruzsinszky, G. I. Csonka, O. A. Vydrov, G. E. Scuseria, L. A. Constantin, X. Zhou and K. Burke, *Phys. Rev. Lett.*, 2008, **100**, 136406.
56 S. Grimme, J. Antony, S. Ehrlich and H. Krieg, *J. Chem. Phys.*, 2010, **132**, 154104.
57 J. M. Skelton, L. A. Burton, F. Oba and A. Walsh, *J. Phys. Chem. C*, 2017, **121**, 6446–6454.
58 I. Pallikara and J. M. Skelton, *Phys. Chem. Chem. Phys.*, 2021, **23**, 19219–19236.
59 P. E. Blöchl, *Phys. Rev. B: Condens. Matter Mater. Phys.*, 1994, **50**, 17953.
60 G. Kresse and D. Joubert, *Phys. Rev. B: Condens. Matter Mater. Phys.*, 1999, **59**, 1758.
61 A. Togo and I. Tanaka, *Scr. Mater.*, 2015, **108**, 1–5.
62 A. Togo, L. Chaput and I. Tanaka, *Phys. Rev. B: Condens. Matter Mater. Phys.*, 2015, **91**, 094306.
63 X. Gonze and C. Lee, *Phys. Rev. B: Condens. Matter Mater. Phys.*, 1997, **55**, 10355.
64 M. Gajdoš, K. Hummer, G. Kresse, J. Furthmüller and F. Bechstedt, *Phys. Rev. B: Condens. Matter Mater. Phys.*, 2006, **73**, 045112.
65 A. V. Krukau, O. A. Vydrov, A. F. Izmaylov and G. E. Scuseria, *J. Chem. Phys.*, 2006, **125**, 224106.
66 A. M. Ganose, J. Park, A. Faghaninia, R. Woods-Robinson, K. A. Persson and A. Jain, *Nat. Commun.*, 2021, **12**, 2222.
67 J. M. Skelton, D. S. Gunn, S. Metz and S. C. Parker, *J. Chem. Theory Comput.*, 2020, **16**, 3543–3557.
68 A. Walsh, D. J. Payne, R. G. Egdell and G. W. Watson, *Chem. Soc. Rev.*, 2011, **40**, 4455–4463.
69 H. Yu, D. Gao, X. Wang, X. Du, X. Lin, W. Guo, R. Zou, C. Jin, K. Li and Y. Chen, *NPG Asia Mater.*, 2018, **10**, 882–887.
70 M. Sist, C. Gatti, P. Nørby, S. Cenedese, H. Kasai, K. Kato and B. B. Iversen, *Chem. – Eur. J.*, 2017, **23**, 6888–6895.
71 L. Ehm, K. Knorr, P. Dera, A. Krimmel, P. Bouvier and M. Mezouar, *J. Phys.: Condens. Matter*, 2004, **16**, 3545.
72 S. Xie, X. Cheng, C. Hu, Y. Tao, M. Liu and Z. Qi, *J. Alloys Compd.*, 2020, **849**, 155915.
73 M. J. Smiles, J. M. Skelton, H. Shiel, L. A. Jones, J. E. Swallow, H. J. Edwards, P. A. Murgatroyd, T. J. Featherstone, P. K. Thakur and T.-L. Lee, *et al.*, *J. Mater. Chem. A*, 2021, **9**, 22440–22452.
74 K. Momma and F. Izumi, *J. Appl. Crystallogr.*, 2011, **44**, 1272–1276.
75 P. Sutter, C. Argyropoulos and E. Sutter, *Nano Lett.*, 2018, **18**, 4576–4583.
76 L. T. Nguyen and G. Makov, *Cryst. Growth Des.*, 2022, **22**, 4956–4969.
77 K. Yuan, Z. Sun, X. Zhang, X. Gong and D. Tang, *Phys. Chem. Chem. Phys.*, 2020, **22**, 1911–1922.
78 J. Yang, Q. Fan, B. Xiao and Y. Ding, *Materials*, 2019, **12**, 3612.
79 V. L. Deringer, R. P. Stoffel and R. Dronskowski, *Phys. Rev. B: Condens. Matter Mater. Phys.*, 2014, **89**, 094303.
80 J. M. Skelton, D. Tiana, S. C. Parker, A. Togo, I. Tanaka and A. Walsh, *J. Chem. Phys.*, 2015, **143**, 064710.
81 J. M. Skelton, S. C. Parker, A. Togo, I. Tanaka and A. Walsh, *Phys. Rev. B: Condens. Matter Mater. Phys.*, 2014, **89**, 205203.
82 C. Kannewurf and R. Cashman, *J. Phys. Chem. Solids*, 1961, **22**, 293–298.
83 A. Elkorashy, *J. Phys. C-Solid State Phys.*, 1988, **21**, 2595.
84 P. Ramasamy, D. Kwak, D.-H. Lim, H.-S. Ra and J.-S. Lee, *J. Mater. Chem. C*, 2016, **4**, 479–485.
85 P. A. Murgatroyd, M. J. Smiles, C. N. Savory, T. P. Shalvey, J. E. Swallow, N. Fleck, C. M. Robertson, F. Jackel, J. Alaria and J. D. Major, *et al.*, *Chem. Mater.*, 2020, **32**, 3245–3253.
86 E. Segev, U. Argaman, R. E. Abutbul, Y. Golan and G. Makov, *CrystEngComm*, 2017, **19**, 1751–1761.
87 G. K. Madsen, J. Carrete and M. J. Verstraete, *Comput. Phys. Commun.*, 2018, **231**, 140–145.
88 G. K. Madsen, J. Carrete and M. J. Verstraete, *Comput. Phys. Commun.*, 2018, **231**, 140–145.
89 T. Lyu, X. Li, Q. Yang, J. Cheng, Y. Zhang, C. Zhang, F. Liu, J. Li, W. Ao and H. Xie, *et al.*, *Chem. Eng. J.*, 2022, **442**, 136332.
90 X. Shi, Z.-G. Chen, W. Liu, L. Yang, M. Hong, R. Moshwan, L. Huang and J. Zou, *Energy Storage Mater.*, 2018, **10**, 130–138.
91 X. Shi, A. Wu, T. Feng, K. Zheng, W. Liu, Q. Sun, M. Hong, S. T. Pantelides, Z.-G. Chen and J. Zou, *Adv. Energy Mater.*, 2019, **9**, 1803242.
92 I. Suzuki, S. Kawanishi, T. Omata and H. Yanagi, *JPhys: Energy*, 2022, **4**, 042002.
93 X. Yang, W.-H. Gu, W.-J. Li, Y.-X. Zhang, J. Feng and Z.-H. Ge, *J. Phys. Chem. Solids*, 2023, **172**, 111077.

94 C. W. Li, J. Hong, A. F. May, D. Bansal, S. Chi, T. Hong, G. Ehlers and O. Delaire, *Nat. Phys.*, 2015, **11**, 1063–1069.
95 J. M. Skelton, L. A. Burton, S. C. Parker, A. Walsh, C.-E. Kim, A. Soon, J. Buckeridge, A. A. Sokol, C. R. A. Catlow, A. Togo and I. Tanaka, *Phys. Rev. Lett.*, 2016, **117**, 075502.
96 U. Aseginolaza, R. Bianco, L. Monacelli, L. Paulatto, M. Calandra, F. Mauri, A. Bergara and I. Errea, *Phys. Rev. Lett.*, 2019, **122**, 075901.
97 J. M. Skelton, *J. Mater. Chem. C*, 2021, **9**, 11772–11787.
98 K. Yuan, Z. Sun, X. Zhang and D. Tang, *Sci. Rep.*, 2019, **9**, 9490.
99 Q. Fan, J. Yang, J. Cao and C. Liu, *R. Soc. Open Sci.*, 2021, **8**, 201980.
100 G. Ding, G. Gao and K. Yao, *Sci. Rep.*, 2015, **5**, 9567.
101 H. L. Kagdada, P. K. Jha, P. Spiewak, K. J. Kurzydłowski and D. K. Singh, *J. Appl. Phys.*, 2020, **127**, 175104.
102 W. Liu, K. C. Lukas, K. McEnaney, S. Lee, Q. Zhang, C. P. Opeil, G. Chen and Z. Ren, *Energy Environ. Sci.*, 2013, **6**, 552–560.
103 Y.-M. Han, J. Zhao, M. Zhou, X.-X. Jiang, H.-Q. Leng and L.-F. Li, *J. Mater. Chem. A*, 2015, **3**, 4555–4559.
104 Asfandiyar, T.-R. Wei, Z. Li, F.-H. Sun, Y. Pan, C.-F. Wu, M. U. Farooq, H. Tang, F. Li and B. Li, *et al.*, *Sci. Rep.*, 2017, **7**, 43262.
105 C.-C. Lin, R. Lydia, J. H. Yun, H. S. Lee and J. S. Rhyee, *Chem. Mater.*, 2017, **29**, 5344–5352.
106 F. Ke, J. Yang, C. Liu, Q. Wang, Y. Li, J. Zhang, L. Wu, X. Zhang, Y. Han and B. Wu, *et al.*, *J. Phys. Chem. C*, 2013, **117**, 6033–6038.
107 K. Adouby, C. Perez-Vicente, J. Jumas, R. Fourcade and A. A. Toure, *Z. Kristallogr. - Cryst. Mater.*, 1998, **213**, 343–349.
108 T. Chattopadhyay, J. Pannetier and H. G. Von Schnering, *J. Phys. Chem. Solids*, 1986, **47**, 879–885.
109 M.-S. Lee and S. D. Mahanti, *Phys. Rev. B: Condens. Matter Mater. Phys.*, 2012, **85**, 165149.
110 W. He, D. Wang, J.-F. Dong, Y. Qiu, L. Fu, Y. Feng, Y. Hao, G. Wang, J. Wang, C. Liu, J.-F. Li, J. He and L.-D. Zhao, *J. Mater. Chem. A*, 2018, **6**, 10048–10056.
111 J. Flitcroft, A. Althubiani and J. Skelton, *ChemRxiv*, 2023, preprint, DOI: **10.26434/chemrxiv-2023-lh90f**.
112 A. S. Chaves, D. T. Larson, E. Kaxiras and A. Antonelli, *Phys. Rev. B*, 2022, **105**, 205201.